



# Edge modes and their conductance in narrow nanoribbons of 2D materials in a topological phase

Viktor Sverdlov<sup>a,b,\*</sup>, Heribert Seiler<sup>a,b</sup>, Al-Moatasem Bellah El-Sayed<sup>b</sup>, Yury Illarionov<sup>a,c</sup>, Hans Kosina<sup>b</sup>

<sup>a</sup> Christian Doppler Laboratory for Nonvolatile Magnetoresistive Memory and Logic at the Institute for Microelectronics, TU Wien, Gußhausstraße 27-29, A-1040 Wien, Austria

<sup>b</sup> Institute for Microelectronics, TU Wien, Gußhausstraße 27-29, A-1040 Wien, Austria

<sup>c</sup> Ioffe Physical-Technical Institute, Polytechnicheskaya 26, St-Petersburg, 194021, Russia

## ARTICLE INFO

Handling Editor Bogdan Cretu

### Keywords:

Topologically protected edge states

Topological insulators

Nanoribbons

$k \cdot p$  method

Conductance

## ABSTRACT

Employing novel 2D materials with topologically protected current-carrying edge states is promising to boost the on-current in electronic devices. Using nanoribbons is essential to reduce the contribution of the 2D bulk states to the current. Making the nanoribbon widths narrower allows one to put more current-carrying edge states under the gate of a fixed width thus increasing the current. However, the edge states from opposite edges may start to interact in narrow nanoribbons. Based on an effective  $k \cdot p$  model, we analyze the topologically protected edge states and their conductance for several 2D materials as a function of the normal electric field. We compare the 2D materials  $\text{MoS}_2$ ,  $\text{MoSe}_2$ ,  $\text{WS}_2$ , and  $\text{WSe}_2$  in the topological  $1T'$  phase and find the largest electric field-induced conductance modulation in  $\text{MoS}_2$  nanoribbons.

## 1. Introduction

Exploiting novel materials with advanced properties is mandatory to continue with the device scaling for high performance applications at reduced power. Topological insulators (TIs) belong to a class of materials which possess new properties not available in other materials: namely, highly conductive edge states with a nearly linear dispersion that are topologically protected and hence immune to backscattering. Therefore, it is highly attractive to use these conductive edge states to carry the on-current in novel devices. It is important that the edge states lie within the fundamental band gap of these new materials. Applying a gate voltage allows one to move the Fermi level from the gap in the conduction or the valence bands where there is strong scattering between the edge and the bulk electron or hole states [1]. This leads to a substantial reduction of the current, resulting in an on/off current ratio suitable for device applications [1].

Recently, it was predicted by *ab initio* calculations that well-known monolayer-thin two-dimensional (2D) materials with high promise for future microelectronic devices [2] can also be found in a  $1T'$  TI phase [3]. The band gap is opened by the spin-orbit interaction at the intersections (degeneracy points) between the inverted electron and hole

bands. As this is the gap between the inverted bands, the existence of very peculiar states lying in the gap is expected [3]. These states are localized at the edge and are characterized by a property that is very attractive for application: spin-momentum locking property: It turns out that the two otherwise degenerate edge states with opposite spin orientations propagate in opposite directions along the edges. Therefore, running the current along the edge through the edge states results in its almost perfect spin polarization. The spin-polarized currents are known to be the key to enable writing data in emerging magnetoresistive random access memories [4,5]. The edge states are predicted to be protected against backscattering [6] and are therefore expected to perfectly carry the current even at nonideal edges typical to experiments.

The value of the gap can be modulated by an external electric field  $E_z$  applied normal to the 2D sheet. The band gap in the inverted band structure is reduced and can be completely closed upon increasing values of  $E_z$  [3]. By further increasing  $E_z$  the band gap reopens again; however, the traditional electron and hole band order is restored indicating a topological phase transition from a non-trivial topological to a trivial insulator. In contrast to the TI phase where the highly conductive edge states exist and can carry a large current, no current-carrying edge

\* Corresponding author.

E-mail address: [Sverdlov@iue.tuwien.ac.at](mailto:Sverdlov@iue.tuwien.ac.at) (V. Sverdlov).

<https://doi.org/10.1016/j.sse.2022.108266>

states are allowed within the band gap of the trivial insulating phase, so there is no current due to the edge states. Therefore, the normal electric field induced topological phase transition between the TI and the trivial insulating phases offers a way alternative to the one in [1] to modulate the current by the gate voltage and to design new current switches.

If the current is carried only through the edge states located at the edges of a 2D sheet, it is quite small regardless of the high conductance and the absence of backscattering of the edge states. To enhance the on-current due to the edge states it is mandatory to have many edges. One can achieve this by placing several narrower nanoribbons under the gate of the same width. The narrower the nanoribbon is, the more nanoribbons one can assemble. At the same time, the contribution due to the 2D bulk states capable to backscatter decreases due to the size quantized bandgap increase with shrinking nanoribbon width [7].

However, the behaviour of the edge states in a narrow nanoribbon can differ from that at the edge of an infinite 2D sheet. Indeed, a small gap in the gapless spectrum of the edge states opens due to an interaction between the topologically protected states from the opposite edges [8,9]. Because of this gap in the dispersion of the edge modes, their conductance was found to be slightly less than the ideal conductance  $G_0 = 2e^2/h$ .

In this work we improve and generalize our numerical approach [10] to handle a broad range of 2D materials. We evaluate the edge states and their corresponding ballistic Landauer conductances in nanoribbons of several 2D materials in the 1T' TI phase. In addition to MoS<sub>2</sub> we consider MoSe<sub>2</sub>, WS<sub>2</sub>, and WSe<sub>2</sub> and critically compare the results. The work was presented at the 7th Joint International EuroSOI Workshop and International Conference on Ultimate Integration on Silicon (EuroSOI-ULIS'2021) [11].

## 2. Method

The subbands in a nanoribbon of a topological 2D material are found numerically following the approach described in [10]. The unknown vector  $\mathbf{x} = (k_1, k_2, k_3, k_4, E)^T$  which includes the subband energy  $E$  is found by solving a nonlinear equation system of the form.

$$\mathbf{F}(\mathbf{x}) = 0. \quad (1)$$

The vector-valued function  $\mathbf{F}$  is composed of the following components:

$$\begin{aligned} F_1 &= k_1 k_2 k_3 k_4 - a_0 \\ F_2 &= k_1 k_2 k_3 + k_1 k_2 k_4 + k_1 k_3 k_4 + k_2 k_3 k_4 + a_1 \\ F_3 &= k_1 k_2 + k_1 k_3 + k_1 k_4 + k_2 k_3 + k_2 k_4 + k_3 k_4 - a_2 \\ F_4 &= k_1 + k_2 + k_3 + k_4 \\ F_5 &= \det(\mathbf{M}) \end{aligned} \quad (2)$$

The first four equations,  $F_i = 0, i = 1, 2, 3, 4$ , represent Vieta's relations between the four roots  $k_1, \dots, k_4$  of a quartic equation

$$k_y^4 + a_2 k_y^2 + a_1 k_y + a_0 = 0. \quad (3)$$

The coefficients  $a_m, m = 0, 1, 2$  in (3) are determined from the characteristic equation [10]

$$\det(H(\mathbf{k}) - E\mathbf{I}) = 0 \quad (4)$$

with  $\mathbf{I}$  being the  $2 \times 2$  unit matrix and

$$H(\mathbf{k}) = \begin{pmatrix} \frac{1}{2} - k_y^2 \frac{m}{m_y^p} - k_x^2 \frac{m}{m_x^p} & \nu_2 k_y - \alpha E_z + i\nu_1 k_x \\ \nu_2 k_y - \alpha E_z - i\nu_1 k_x & -\frac{1}{2} + k_y^2 \frac{m}{m_y^d} + k_x^2 \frac{m}{m_x^d} \end{pmatrix}. \quad (5)$$

Here  $H(\mathbf{k})$ ,  $\mathbf{k} = (k_x, k_y)$  is the spin-up Hamiltonian determining the bulk bands dispersion in an infinite 2D sheet in a topological 1T' material. For convenience (4) is written in dimensionless units: All energies are measured in units of the separation  $\delta$  between the electron and hole bulk bands at the  $\Gamma$ -point, while the components of the wave vectors  $\mathbf{k} =$

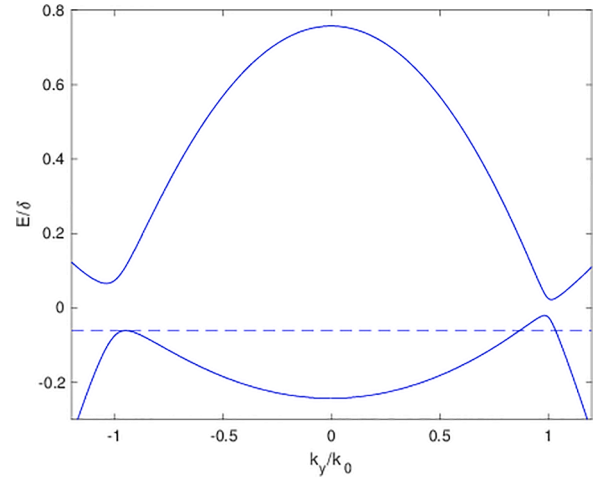


**Fig. 1.** Bulk bands  $\mathbf{k} \cdot \mathbf{p}$  dispersion in a 1T' MoS<sub>2</sub> 2D sheet at  $E_z = \alpha^{-1} \nu_2 / 2$  and  $k_x = 0$ . Dashed line touches an extremum of dispersions discussed later in the text.

$(k_x, k_y)$  are in units  $k_0 = \left( \frac{2\delta}{\hbar^2} \frac{m_y^d m_x^p}{m_y^d + m_x^p} \right)^{1/2}$ . In (5)  $m_{y(x)}^{d(p)}$  are the effective

masses,  $m = \frac{m_y^d m_x^p}{m_y^d + m_x^p}$ ,  $\nu_{1(2)}$  are the dimensionless velocities characterizing the strength of the spin-orbit interaction and  $E_z$  is the electric field normal to the sheet of a 2D material.

Solved with respect to  $E$  dependent on  $\mathbf{k} = (k_x, k_y)$ , (3) determines the energy bands' dispersion in an infinite sheet of a 2D material. The bulk dispersion is characterized by the inverted band structure such that the electron-like band lies below the hole like one at the  $\Gamma$ -point as illustrated in Fig. 1 for MoS<sub>2</sub> and  $k_x = 0$ . Without the spin-orbit interaction ( $\nu_1 = \nu_2 = 0$ ) the electron and hole bulk bands are intersecting at  $k_y = \pm k_0$  explaining the choice of  $k_0$  to measure the wave vectors in (4). The finite spin-orbit interaction opens the fundamental gap at  $k_y$  around  $k_0$ . The dispersion relations and the wave functions for the spin-down states are obtained from the spin-up solutions by applying the time reversal symmetry operation which inverts the spin orientation and the momentum  $\mathbf{k}$  direction simultaneously [5].

It then follows that the first four equations in (2) guarantee that  $k_y = k_1, \dots, k_4$  and  $E$  satisfy the bulk dispersion relations at a fixed  $k_x$ . The last equation in (1),  $F_5 = 0$ , serves to select only the pairs  $(k_y, E)$  which also satisfy the infinite square well potential boundary conditions for the wave function in a nanoribbon of the width  $d$  [10]:

$$\Psi(y = (d/2 \pm d/2)) = 0. \quad (6)$$

In (2) the matrix  $\mathbf{M} = (\mathbf{m}_1, \mathbf{m}_2, \mathbf{m}_3, \mathbf{m}_4)$  is composed of the four columns  $\mathbf{m}_j$  defined as

$$\mathbf{m}_j = \begin{pmatrix} \xi \\ \eta \\ \xi \exp(ik_j d) \\ \eta \exp(ik_j d) \end{pmatrix}. \quad (7)$$

The pair  $(\xi, \eta)^T$  in (7) is an eigenvector of the Hamiltonian matrix (5) at an energy  $E$  [10].

While solving (1) numerically, special care must be taken of crossings of the solution as a function of a parameter. In addition, special attention must be paid to eliminate spurious solutions of (1) that are not related to edge states or subbands in a nanoribbon [10]. These solutions stem from the extrema of the bulk dispersion relations shown by the dashed line in Fig. 1. At these particular points (1) is automatically satisfied. Indeed, as the extrema belong to the bulk dispersion, they fulfill  $F_i = 0, i = 1, 2, 3, 4$ . Because at the extremum shown in Fig. 1, two

**Table 1**

Parameters [9] used in the model.  $m_e$  is the electron mass,  $e$  is the electron charge.

Variable	MoS <sub>2</sub>	MoSe <sub>2</sub>	WS <sub>2</sub>	WSe <sub>2</sub>
$\delta$ [eV]	0.55	0.76	0.17	0.69
$V_1$ [m/s]	$3.38 \cdot 10^5$	$3.42 \cdot 10^5$	$2.93 \cdot 10^5$	$3.54 \cdot 10^5$
$V_2$ [m/s]	$0.23 \cdot 10^5$	$0.23 \cdot 10^5$	$0.85 \cdot 10^5$	$0.38 \cdot 10^5$
$m_x^p/m_e$	0.48	0.28	0.53	0.36
$m_y^p/m_e$	0.29	0.17	0.28	0.16
$m_x^d/m_e$	2.32	2.65	3.2	3.28
$m_y^d/m_e$	0.92	3.14	8.2	8.4
$\alpha'/e$ [nm]	0.016	0.027	0.017	0.024
$k_0$ [nm <sup>-1</sup> ]	1.8	1.9	1.08	1.7

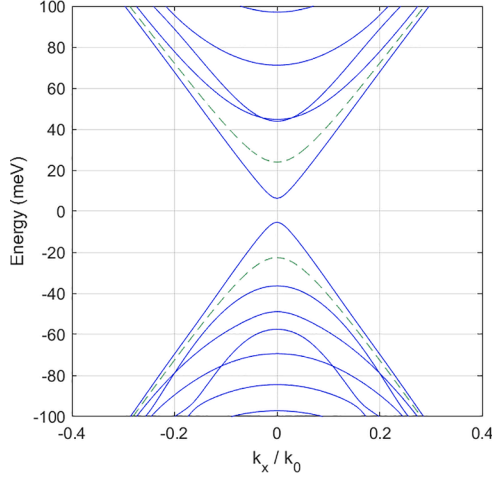


**Fig. 2.** Subband structure in a MoS<sub>2</sub> nanoribbon of width  $d = 20$  nm at  $E_z = 0$ . The subbands with a nearly linear dispersion and a small gap at  $k_x = 0$  correspond to the edge modes. Dashed lines correspond to the extrema of the bulk dispersion satisfying (1,2) and (8).

roots of (3) are equal,  $k_3 = k_4$ , and thus two columns (7) in the matrix  $\mathbf{M}$  become identical, such that  $F_5 = \det(\mathbf{M}) = 0$  is automatically satisfied. Although the extrema of the bulk dispersions are the formal solutions of (1), they do not depend on the nanoribbon's width. The related wavefunctions are identically zero and the  $E$ - $k$  pairs must be disregarded.

In our numerical approach to solve (1) we carefully identify and exclude the spurious solutions based on the following requirement. These solutions correspond to the extrema of the bulk dispersion  $E(k_x, k_y)$  and therefore satisfy

$$\frac{\partial E(k_x, k_y)}{\partial k_y} = 0. \quad (8)$$

In the present paper we extend our study [10] and solve the nonlinear system (1) numerically for a broad range of parameters. In addition to MoS<sub>2</sub> discussed in [10] (but with different material parameters set from [3]), we also study MoSe<sub>2</sub>, WS<sub>2</sub>, and WSe<sub>2</sub>. The parameters used in the calculations as well as the values of  $k_0$  are listed in Table 1. The dimensionless parameters  $v_{1,2}$  and the parameter  $\alpha$  in (5) are related the physical material parameters in Table 1 as  $v_{1,2} = V_{1,2}k_0/\delta$ ,  $\alpha = \alpha'/\delta$ .

### 3. Results

#### 3.1. Subbands dispersions

To evaluate the subband dispersions at a particular value of the electric field, the system (1) is solved numerically as a function of the dimensionless momentum  $k_x$ . We begin with the evaluation of subbands in a 1T' MoS<sub>2</sub> nanoribbon of the width 20 nm cleaved along the OX axis.

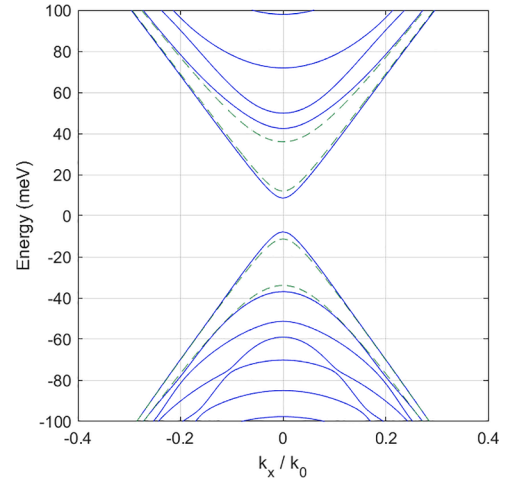


**Fig. 3.** Subband structure in a MoS<sub>2</sub> nanoribbon of width  $d = 20$  nm at the field  $E_z = \alpha^{-1}v_2/2$ . The gap between the electron- and hole-like subbands increases. Dashed lines: extrema of the bulk dispersion.

In contrast to [10], we employ the material parameters [9] (Table 1). In addition to [10], we explicitly show the spurious bands. Moreover, we significantly improved the accuracy of the iteration procedure in order to clearly resolve and distinguish the crossings in the subband dispersions not performed in [10].

Fig. 2 shows the subbands without the normal electric field ( $E_z = 0$ ).

The energies are offset by  $\Delta E = \frac{\delta}{2} \frac{m_y^d - m_x^p}{m_y^d + m_x^p}$  for convenience. The topmost hole-like and the lowest electron-like subbands with almost linear dispersions correspond to the edge states [9,10]. The positions of the extrema of the electron- and hole-like bands close to  $k_0$  (Fig. 1) depend on  $k_x$  and are also shown in Fig. 2 with dashed lines. The bulk bandgap is defined by the minimum energy separating the extrema. Clearly, the edge modes dispersion lies within the bulk bandgap (Fig. 2). A small gap of about 10 meV in an otherwise linear spectrum of the edge modes is due to an interaction of the edge modes localized at opposite edges in a narrow nanoribbon.

In the absence of a normal electric field the roots  $k_1, \dots, k_4$  of (3) corresponding to the edge modes are in the form  $k_j = \pm a \pm ib$ . However, in the Newton algorithm we do not constrain  $k_j$  while solving (1) and vary all four  $k_j$  and the energy  $E$ , for a fixed  $k_x$ , to evaluate  $|\det(\mathbf{M})|$  and bring it below a tolerance of  $10^{-10}$ . Simultaneously we ensure that (3) is fulfilled. Therefore, the degree of asymmetry of the roots  $k_j$  obtained numerically is a good measure of the solver's accuracy. It turns out that for a Newton scheme tolerance of  $10^{-10}$  the relative asymmetry error of the roots  $k_j$  is less than  $10^{-13}$ .

Higher electron and lower hole subbands lie within the bulk conduction or the valence bands. Both, electron and hole subbands, can be separated into two groups with distinct curvatures at small  $k_x$  or to different effective masses. To number the subbands, one can introduce an index within each group of electron and hole subbands. Our numerical analysis demonstrates that there exist simple dispersions crossings between the subbands with the same index from different groups, while anti-crossings appear if the subbands indexes are different.

To differentiate a subband crossing from an anti-crossing, a careful choice of an initial guess for the solution is critical. A poor initial guess may lead to the solution jumping on a different subband nearby, which mistakenly results in an uneven subband dispersion [10]. For the Newton's method to stay on the same solution, we first choose a suitable value for  $E$  at  $k_x = 0$  and solve (1) numerically until a desired accuracy is achieved. For the next  $k_x$  the new starting value  $E$  is obtained by extrapolating the solution vector  $\mathbf{x}$ . Close to the crossing or anti-crossing, a quadratic extrapolation to obtain the next initial guess is required. For results shown in Fig. 2 about 100 linearly spaced  $k_x$  points were used to

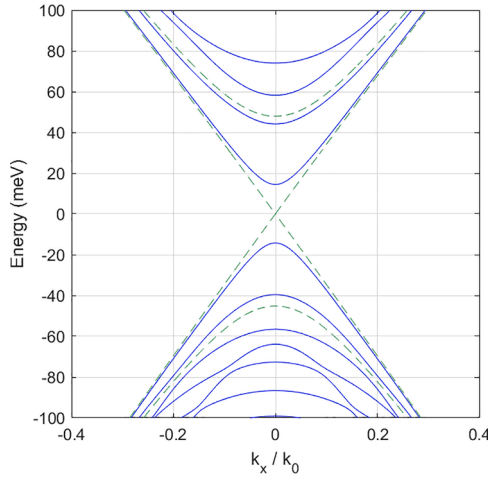


**Fig. 4.** Subband structure in a MoS<sub>2</sub> nanoribbon of width  $d = 20$  nm at the critical field  $E_z = \alpha^{-1}\nu_2$  at which the fundamental gap in a 2D sheet closes. In contrast, the gap in the nanoribbon increases. Dashed lines: extrema of the bulk dispersion.

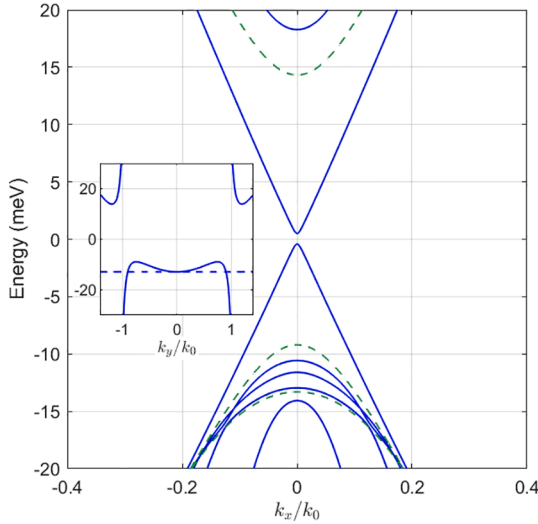


**Fig. 5.** Subband structure in a WSe<sub>2</sub> nanoribbon of width  $d = 10$  nm at  $E_z = 0$ . The subbands with the linear dispersion and a small gap at  $k_x = 0$  correspond to the edge modes. Dashed lines: extrema of the bulk dispersion. The lowest dashed line is due to the minimum of the bulk dispersion at the  $\Gamma$ -point  $k_y = 0$ . Inset: bulk dispersion in WSe<sub>2</sub> at  $E_z = 0$  and  $k_x = 0$ .

preserve the dispersions smooth and to resolve the crossings and anti-crossings of the subbands.

**Fig. 3** demonstrates the subbands in a 20 nm 1T' MoS<sub>2</sub> nanoribbon and the positions of the bulk dispersion extrema at the electric field  $E_z = \alpha^{-1}\nu_2/2$ . If the normal field is present, the bulk dispersion becomes asymmetric as seen in **Fig. 1** displaying two minima and two maxima around  $\pm k_0$  with different energies. The dependences of the four extrema as function of  $k_x$  are shown with dashed lines in **Fig. 3**.

Because of the asymmetry of the bulk dispersion (**Fig. 1**), the subband crossings in the bulk conduction or valence bands transform to anti-crossings as shown in **Fig. 3**. The edge modes dispersion at  $E_z = \alpha^{-1}\nu_2/2$  is still laying within the bulk dispersion gap, however, the separation between the electron- and hole-like edge modes at  $k_x = 0$  becomes larger than at  $E_z = 0$ .

**Fig. 4** shows the subband structure at the normal field  $E_z = E_c = \alpha^{-1}\nu_2$ . This field value is critical for the bulk band structure in an infinite sheet of a 2D material as at this electric field the fundamental band gap

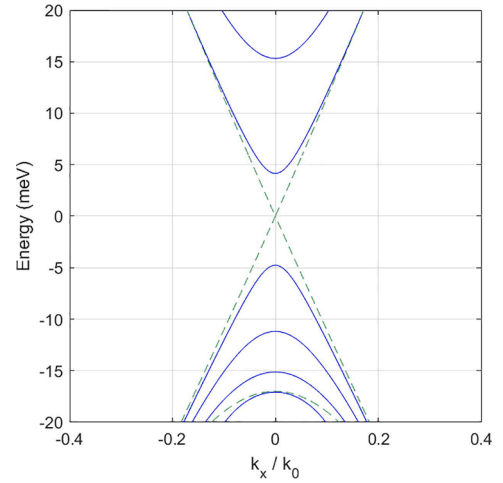


**Fig. 6.** Subband structure in a WSe<sub>2</sub> nanoribbon of width  $d = 10$  nm at  $E_z = \alpha^{-1}\nu_2$ . The subband gap remains finite and keeps increasing with the normal field, in contrast to the bulk bandgap. Dashed lines: extrema of the bulk dispersion.

closes (dashed lines). However, the gap separating the lowest electron-like and highest hole-like subbands at  $k_x = 0$  remains finite and increases even further as compared to the gap at  $E_z = \alpha^{-1}\nu_2/2$ . As there is no fundamental gap in the bulk at  $E_z = \alpha^{-1}\nu_2$ , all subband dispersions are in the bulk conduction or valence band. This leads to a qualitatively different behavior of the edge states wave functions discussed later.

**Fig. 5** shows the subbands and the spurious solutions corresponding to the bulk bands extrema in a WSe<sub>2</sub> nanoribbon of the width of 10 nm at  $E_z = 0$ . The edge modes' dispersions remain almost linear in a broad range of  $k_x$ , with an exception of a very narrow region around  $k_x = 0$  where a small gap of about 1 meV between the edge dispersions opens. Two types of hole subbands with different effective masses are observed. In contrast to the MoS<sub>2</sub> case, due to a much heavier  $m_y^d$  effective mass in WSe<sub>2</sub>, the valence band maxima close to  $k_y = \pm k_0$  are very shallow as the valence band minimum at the  $\Gamma$ -point  $k_y = 0$  is only a few milli-electronvolts away as shown in Inset, **Fig. 5**. We only detected three hole-like subbands, for a nanoribbon of the width of 10 nm, with their maxima located between the bulk valence band minimum and maxima. The lowest hole-like subband lies at the energies below the minimum at the  $\Gamma$ -point  $k_y = 0$ , which explains a steeper dispersion with a smaller effective mass.

At the critical value of the electric field  $E_c = \alpha^{-1}\nu_2$  the band gap in the bulk dispersion closes at  $k_y = k_0$ . The edge modes dispersions are in the bulk conduction and valence bands (**Fig. 6**). **Fig. 6** indicates that, similar to the case of MoS<sub>2</sub> nanoribbons, the gap between the lowest electron-like and topmost hole-like subbands increases, while the fundamental gap is zero. We systematically investigate the dependencies of the edge states energies as a function of the normal field in 1T' MoS<sub>2</sub>, MoSe<sub>2</sub>, WS<sub>2</sub>, and WSe<sub>2</sub> nanoribbons.

### 3.2. Edge states as a function of the normal electric field

To evaluate the dependencies the energies of the electron-like and hole-like edge modes with the normal field, we now solve (1) numerically at  $k_x = 0$  as a function of  $E_z$ . The difficulty we encountered was to numerically separate the edge states close to the spurious bands (8) to exclude [10] the spurious solutions. To do so we begin the Newton iterations and obtain results at  $E_z = 0$ . We then keep  $E_z$  increasing. A suitable initial guess for the next  $E_z$  step is obtained by a quadratic extrapolation of energies obtained at the previous steps. The procedure works well until we reach a vicinity of the edge modes dispersions crossing with spurious solutions. The spurious solutions turn to be so

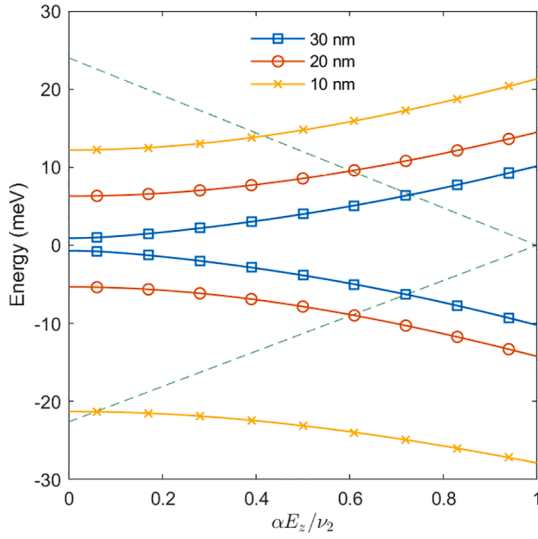


**Fig. 7.** Subband gap dependence in a MoS<sub>2</sub> nanoribbon of width 10 nm (crosses), 20 nm (circles) and 30 nm (squares). The subband gap is larger in narrow nanoribbons and increases with the normal electric field. Dashed lines: spurious solutions [10] due to the extrema of the bulk dispersion.

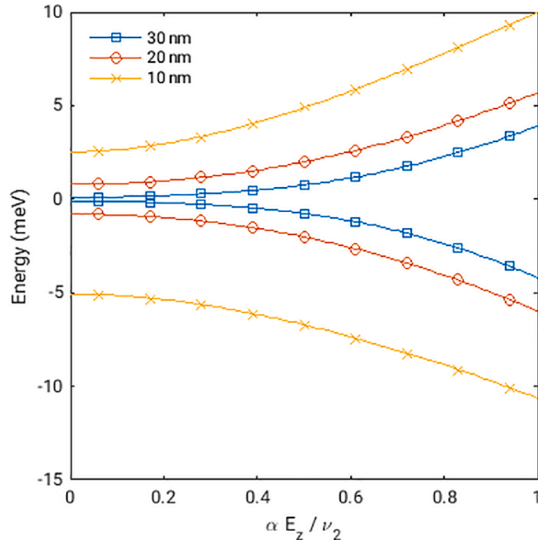


**Fig. 8.** Subband gap dependence in a MoSe<sub>2</sub> nanoribbon of width 10 nm (crosses), 20 nm (circles) and 30 nm (squares) with the normal electric field.

“attractive” that even refining the electric field stepping does not help, and we end on a spurious branch.

To find the lowest electron- and topmost hole-like states at higher  $E_z$  beyond the crossing with the spurious bands, we have chosen a new strategy: we begin at high  $E_z = E_c = \alpha^{-1}\nu_2$  and proceed by stepping  $E_z$  downward until we reach the crossing with the spurious bands. By stitching the solutions continuously across the spurious band, we determine the lowest electron- and topmost hole-like modes as a function of the normal electric field  $E_z$ .

The separation between the lowest electron-like and topmost hole-like edge states and the subband gap increases with the normal electric field for MoS<sub>2</sub> as shown in Fig. 7, for all widths of nanoribbons. The spurious bands are also shown by dashed lines for convenience. The spurious solutions must be excluded [10] as they lead to ambiguous conclusions [9] regarding the subband gap and ballistic conductance. Fig. 8,9 and 10 show the dependencies of the lowest electron-like and the topmost hole-like energies at  $k_x = 0$  as a function of the normal

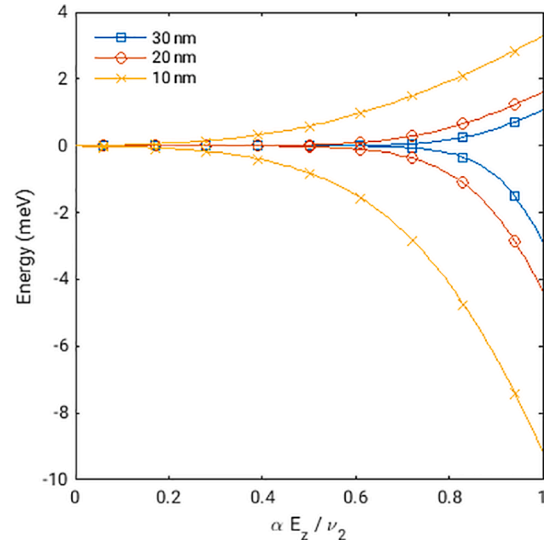


**Fig. 9.** Subband gap dependence in a WS<sub>2</sub> nanoribbon of width 10 nm (crosses), 20 nm (circles) and 30 nm (squares) with the normal electric field.

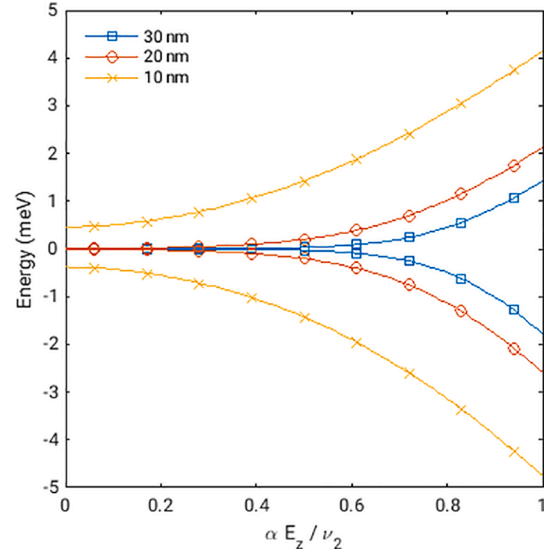


**Fig. 10.** Subband gap dependence in a WSe<sub>2</sub> nanoribbon of width 10 nm (crosses), 20 nm (circles) and 30 nm (squares) with the normal electric field.

electric field in nanoribbons of MoS<sub>2</sub>, WS<sub>2</sub>, and WSe<sub>2</sub>, respectively, for three different widths of 10 nm, 20 nm, and 30 nm. Although the dependencies are varying for different materials, they display three common features, namely: 1) The gap between the edge dispersions increases with the increase of the normal field; 2) the subband spectrum remains gapped even at the critical electric  $E_z = \alpha^{-1}\nu_2$ ; and 3) the gap value is larger for narrower nanoribbons. These results will later be employed to compare the edge mode ballistic conductances in different materials.

### 3.3. Topological phase transition in a nanoribbon

2D topological insulators are characterized by a non-trivial topological order which results in the existence of symmetry protected edge Dirac modes with linear dispersion lying in the fundamental band gap of the insulator. Closing the fundamental gap in the bulk 2D by increasing the normal electric field and reopening it again at higher fields, with the normal noninverted band order restored, represents the transition



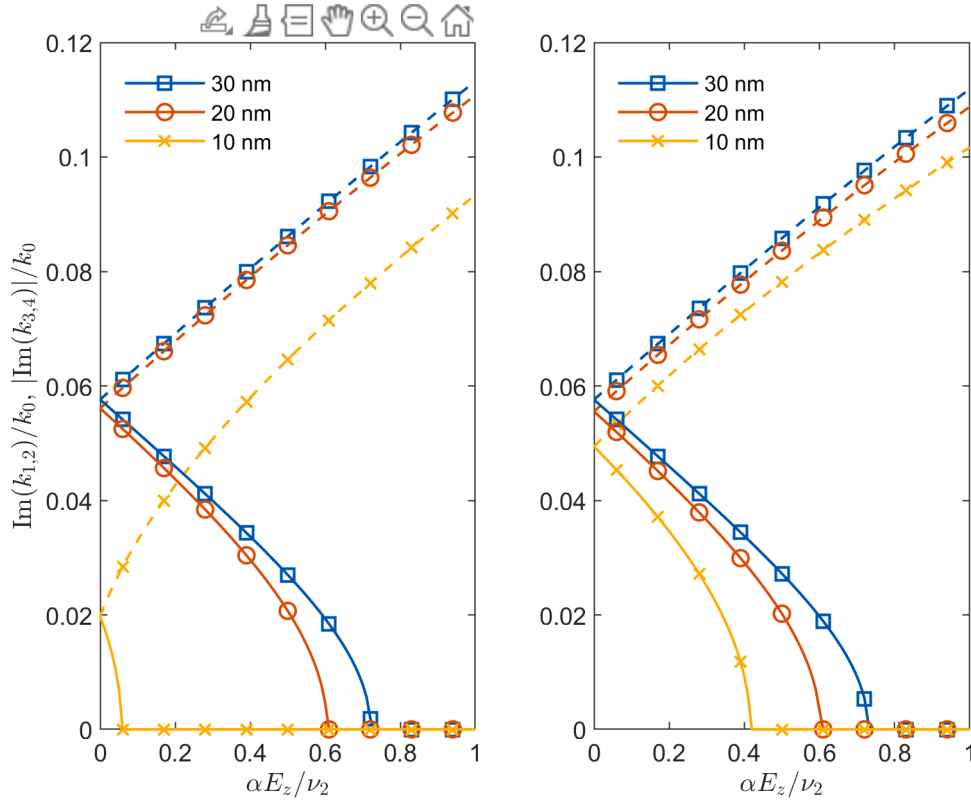


**Fig. 11.** Imaginary part of  $k_{1,2}$  (dashed) and  $k_{3,4}$  (solid) as a function of the normal electric field in a MoS<sub>2</sub> nanoribbon of width 10 nm (crosses), 20 nm (circles) and 30 nm (squares), for hole-like (left panel) and electron-like edge states (right panel).

between the TI and trivial insulator phases [3,9].

We found that in a nanoribbon the behavior of the subband gap with the electric field is opposite to that of the fundamental gap in an infinite 2D sheet of the same material. The question arises if and how one can define a phase transition between the TI and a trivial insulator phase in a nanoribbon.

It is convenient to define a topological transition in a confined nanoribbon geometry based on the properties of the edge states wave function [9,10]

$$\Psi(y) = \sum_{j=1}^4 C_j \begin{pmatrix} \xi \\ \eta \end{pmatrix} \exp(ik_j y). \quad (9)$$

Using a MoS<sub>2</sub> nanoribbon as an example, we demonstrate how this definition works and what its physical consequences are.

If the edge states energies lie within the fundamental gap of a TI (i.e. between the dashed lines in Fig. 7), all  $k_1, \dots, k_4$  in (9) are complex and possess imaginary parts. The inverses of these imaginary parts define the localization length of the wave function at the edges within a nanoribbon [9,10]. Therefore, the states with energies within the fundamental gap are localized at the edge.

With the electric field increasing, the subbands' energies approach the fundamental band gap boundaries (Fig. 7, dashed lines). Fig. 11 demonstrates that while the imaginary part  $b_1$  of  $k_{1,2} = -a_1 \pm ib_1$  increases, the imaginary part  $b_3$  of  $k_{3,4} = a_3 \pm ib_3$  decreases and becomes zero exactly at the electric field corresponding to the crossing of the edge mode dispersion and the bulk bands. As the localization of the wave function qualitatively changes at this value of the electric field, one can define this point as a topological transition in a confined geometry [12].

The electric field at which the character of the wave function (9) changes is not the same for the edge states with the electron- and hole-like dispersions. The values of the electric field at which the transition occurs also depend on the width of nanoribbon: with the nanoribbon

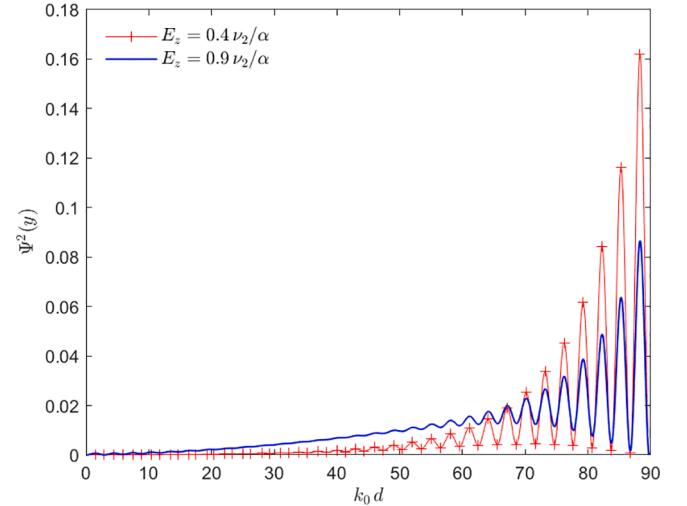


**Fig. 12.** The wave function of the electron-like edge states in a MoS<sub>2</sub> nanoribbon of the width 50 nm, at  $E_z = 0.4\alpha^{-1}\nu_2$  (line with crosses, still localized at the edge) and  $E_z = 0.9\alpha^{-1}\nu_2$  (solid line, substantially delocalized),  $k_x = 0.1k_0$ .

width increasing, the electric field value also increases. However, following this definition the correct value of the critical field  $E_z = E_c = \alpha^{-1}\nu_2$  for an infinitely wide 2D sheet is recovered.

Although the wave function with real  $k_3, k_4$  cannot be considered as localized at the edges, it is not easy to visually distinguish [12] a weak exponential decay from a difference between two sine functions with close frequencies in nanoribbons narrower than 50 nm. Fig. 12 demonstrates the wave functions at two electric field values before and after the topological transition in a MoS<sub>2</sub> nanoribbon of the width 50 nm: While at  $E_z = 0.4\alpha^{-1}\nu_2$  the wave function is clearly localized at the right

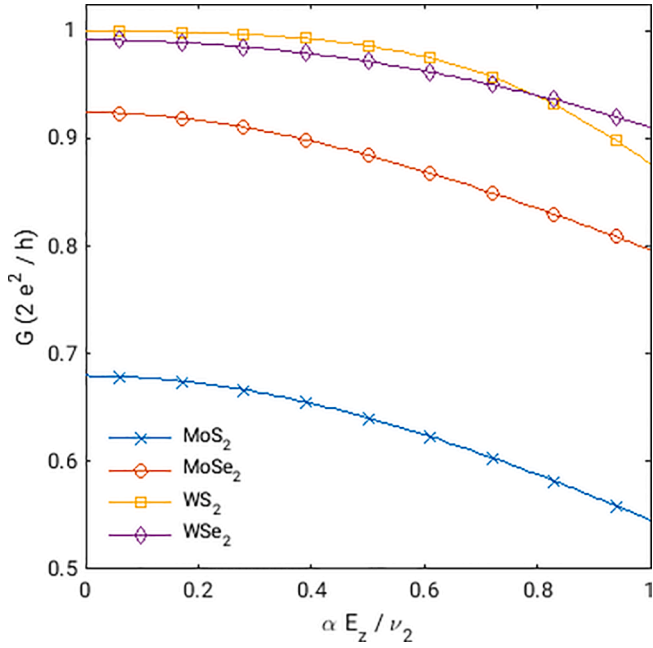


**Fig. 13.** Ballistic conductance (10) as a function of the normal electric field at  $T = 300$  K,  $E_F = 0$  in nanoribbons of the widths 10 nm, for several materials: MoS<sub>2</sub> (crosses), MoSe<sub>2</sub> (circles), WS<sub>2</sub> (squares), and WSe<sub>2</sub> (diamonds).

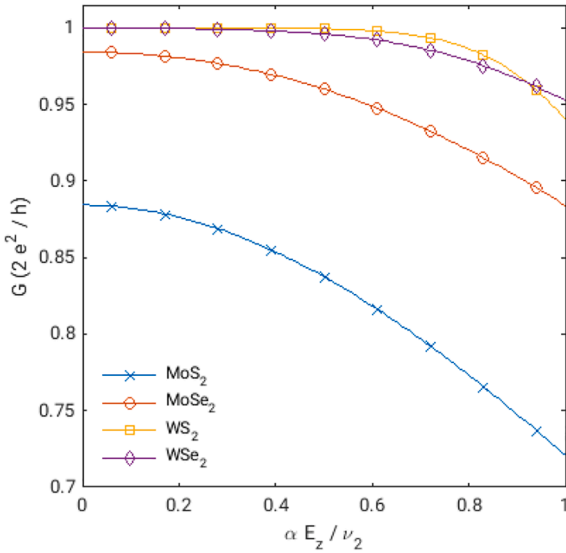


**Fig. 14.** Ballistic conductance (10) as a function of the normal electric field at  $T = 300$  K,  $E_F = 0$  in nanoribbons of the width 20 nm, for several materials: MoS<sub>2</sub> (crosses), MoSe<sub>2</sub> (circles), WS<sub>2</sub> (squares), and WSe<sub>2</sub> (diamonds).

edge and displays an exponential decay superimposed on oscillations, the state at  $E_z = 0.9\alpha^{-1}\nu_2$  shows a clear increase of the electron density in the middle of the nanoribbon away from the edges.

The lowest electron- and topmost hole-like subbands do not abruptly terminate at  $E_z = \alpha^{-1}\nu_2$  and continue to higher values of the normal electric field [10]. However, being delocalized, the states at higher fields become prone to backscattering [12], and do not contribute to the ballistic conductance considered next.

### 3.4. Ballistic conductance due to edge modes

The intriguing property of the edge modes is their symmetry protection against backscattering. The transport due to the edge modes is

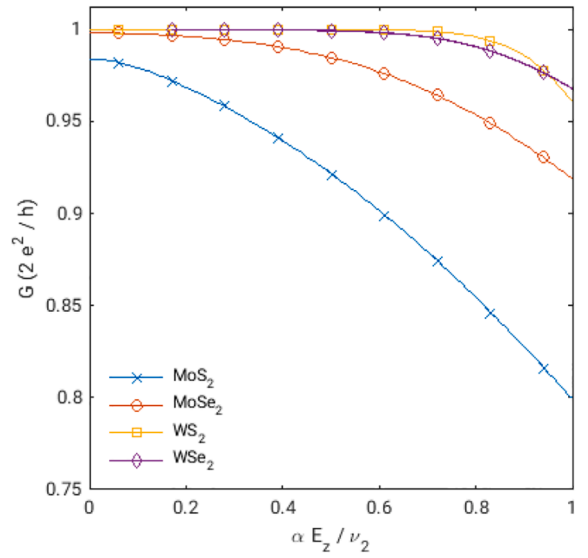


**Fig. 15.** Ballistic conductance (10) as a function of the normal electric field at  $T = 300$  K,  $E_F = 0$  in nanoribbons of the widths 30 nm, for several materials: MoS<sub>2</sub> (crosses), MoSe<sub>2</sub> (circles), WS<sub>2</sub> (squares), and WSe<sub>2</sub> (diamonds).

therefore ballistic. The conductance  $G$  due to the edge modes can be computed by employing the Landauer expression

$$G = \frac{2e^2}{h} \left[ \left( \exp \left\{ \frac{E_0^e - E_F}{k_B T} \right\} + 1 \right)^{-1} + \left( \exp \left\{ \frac{E_F - E_0^h}{k_B T} \right\} + 1 \right)^{-1} \right], \quad (10)$$

where  $E_0^e$  and  $E_0^h$  are the energies of the bottom of the electron-like and the top of the hole-like edge modes, respectively,  $T$  is the temperature and  $E_F$  is the Fermi energy.

The ballistic conductances due to the edge states at room temperature  $T = 300$  K in MoS<sub>2</sub>, MoSe<sub>2</sub>, WS<sub>2</sub>, and WSe<sub>2</sub> 2D nanoribbons in 1T' topological phase as a function of the normal electric field are shown in Fig. 13 for the widths of 10 nm, 20 nm (Fig. 14), and in 30 nm (Fig. 15),  $E_F = 0$ . The conductance decreases with the normal electric field increase for all nanoribbons' widths and all nanoribbons' materials considered. This agrees with Figs. 7-10 demonstrating an increase of the electron- and hole-like edge states energies ( $E_0^{e,h} - E_F$ ) relative to the Fermi level  $E_F = 0$  with the electric fields, for all nanoribbons. For all widths considered, the largest conductance modulation is obtained in MoS<sub>2</sub> nanoribbons. The conductance modulations in nanoribbons of other materials is about 10% or less if the field is increased up to the critical value  $E_c$  corresponding to the transition to the trivial phase in an infinite 2D sheet.

The energies of the electron and hole subbands originating from the edge states continue to increase beyond the critical field  $E_c$  value [10] resulting in a continuous decrease of the ballistic conductance with the electric field. As the wave functions (9) of the electron and hole states at  $E_z > E_c$  gets delocalized from the edges, the states become prone to backscattering [12]. The backscattering will further suppress the conductance and increase the on-off ratio.

The higher electron and lower hole subbands dispersions are lying in the bulk conduction or valence bands. Their wave functions are not protected against backscattering, and their contribution into the ballistic conductance at is small, at  $E_F = 0$  and room temperatures. A viable option to suppress the conductance in the off-state is to push the Fermi level into the bulk conduction or valence bands by applying a gate voltage [1] as intensive intra- and intersubband scattering may result in an on-off ratio of a few orders of magnitude on-off ratio. However, a careful analysis of higher subbands and scattering mechanisms is beyond the scope of the current work.

As the value of the conductance  $G$  is determined by the separations

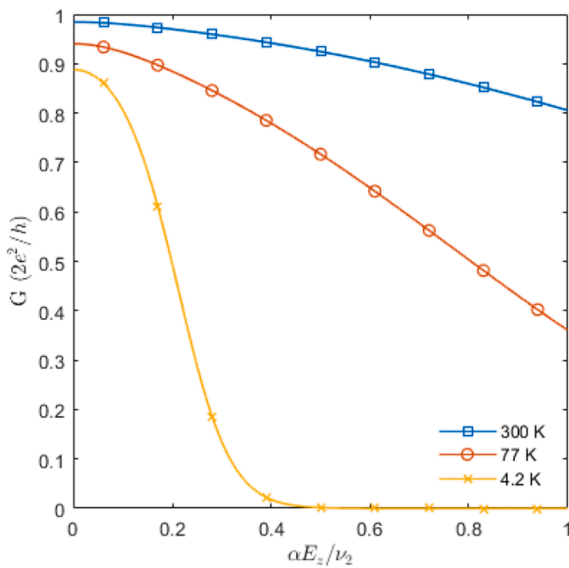


**Fig. 16.** Ballistic conductance (10) as a function of the normal electric field in a MoS<sub>2</sub> nanoribbon of the widths 30 nm,  $E_F = 1.7$  meV, for several temperatures: 300 K (squares), 77 K (circles), 4.2 K (crosses). Subband gap dependence in a MoS<sub>2</sub> nanoribbon of width 10 nm (yellow), 20 nm (red) and 30 nm (blue). The subband gap is larger in narrow nanoribbons and increases with the normal field. (For interpretation of the references to colour in this figure legend, the reader is referred to the web version of this article.)

( $E_0^{e,h} - E_F$ ) relative to  $k_B T$ , a larger subband gap in MoS<sub>2</sub> compared to other results in a lower conductance if  $E_F = 0$ , especially in narrow MoS<sub>2</sub> nanoribbons. The conductance at  $E_z = 0$  can be increased by moving the Fermi level above the bottom of the electron-like/below the top of the hole-like edge mode by a few  $k_B T$ . In order to benefit from the absence of the backscattering, the Fermi level must still lie in the fundamental TI gap. To achieve a high on–off ratio solely due to the edge states, a rapid subband gap increase ( $E_0^e - E_0^h$ ) with the normal field to several  $k_B T$  is required at  $E_z < E_c$ . Fig. 16 demonstrates the ballistic conductance behavior in a MoS<sub>2</sub> nanoribbon with the width of 30 nm and  $E_F = 1.7$  meV at room, liquid nitrogen, and liquid helium temperatures. The conductance at 300 K is not affected by a change of  $E_F$  of 1.7 meV as it is much smaller than  $k_B T \approx 25$  meV. Finally, the conductance at 4.2 K displays an excellent on–off ratio as both requirements to have large conductance at  $E_z = 0$  and a large subband gap compared to  $k_B T$  at  $E_z < E_c$  are satisfied in a MoS<sub>2</sub> nanoribbon at a cryogenic temperature.

#### 4. Conclusion

Edge states in narrow nanoribbons of several transition metal dichalcogenide monolayers in a 1T' topological phase including MoS<sub>2</sub>, MoSe<sub>2</sub>, WS<sub>2</sub>, and WSe<sub>2</sub> are analyzed based on a numerical solution of the dispersion equation obtained with an effective  $\mathbf{k} \cdot \mathbf{p}$  Hamiltonian. It is found that, although a particular value of the subband gap separating the electron- and hole-like edge states depends on the nanoribbon's width and on the material, the subband gap keeps increasing with the value of the normal electric field applied to the nanoribbon.

The increase of the subband gap with the field has got a profound impact on the ballistic transport due to topologically protected edge states. Namely, the ballistic conductance decreases all the way to the critical field when the bulk fundamental gap closes and beyond,

provided the band structure can still be described by an effective  $\mathbf{k} \cdot \mathbf{p}$  Hamiltonian. Among all transition metal dichalcogenide monolayers considered, MoS<sub>2</sub> nanoribbons demonstrate the largest subband gap increase with the normal field and the electric field-induced conductance modulation which can be considered for potential application in ultra-scaled devices at room and cryogenic temperatures.

#### Declaration of Competing Interest

The authors declare that they have no known competing financial interests or personal relationships that could have appeared to influence the work reported in this paper.

#### Acknowledgement

Financial support by the Austrian Federal Ministry for Digital and Economic Affairs, the National Foundation for Research, Technology and Development and the Christian Doppler Research Association is gratefully acknowledged. The authors acknowledge TU Wien Bibliothek for financial support through its Open Access Funding Program.

#### References

- [1] Vandenbergh WG, Fischetti MV. Imperfect two-dimensional topological insulator field-effect transistors. *Nat Commun* 2017;8:1–8. <https://doi.org/10.1038/ncomms14184>.
- [2] Illarionov YY, Banskchikov AG, Polyushkin DK, Wachter S, Knobloch T, Thesberg M, et al. Ultrathin calcium fluoride insulators for two-dimensional field-effect transistors. *Nat Electron* 2019;2:230–5. <https://doi.org/10.1038/s41928-019-0256-8>.
- [3] Qian X, Liu J, Fu L, Li Ju. Quantum spin Hall effect in two-dimensional transition metal dichalcogenides. *Science* 2014;346(6215):1344–7. <https://doi.org/10.1126/science.1256815>.
- [4] Apalkov D, Dieny B, Slaughter JM. Magnetoresistive random access memory. *Proc IEEE* 2016;104:1796–830. <https://doi.org/10.1109/JPROC.2016.2590142>.
- [5] Shao Q, Li P, Liu L, Yang H, Fukami S, Razavi A, et al. Roadmap of Spin–Orbit Torques. *IEEE Trans Magn* 2021;57(7):1–39.
- [6] Hasan MZ, Kane CL. Colloquium: Topological insulators. *RevModPhys* 2010;82:3045–67. <https://doi.org/10.1103/RevModPhys.82.3045>.
- [7] Gilbert MJ. Topological electronics. *Commun Phys* 2021;4(1).
- [8] Zhou B, Lu H-Z, Chu R-L, Shen S-Q, Niu Q. Finite size effects on helical edge states in a quantum spin-Hall system. *Phys Rev Lett* 2008;101:1–4. <https://doi.org/10.1103/PhysRevLett.101.246807>.
- [9] Das B, Sen D, Mahapatra S. Tuneable quantum spin Hall states in confined 1T' transition metal dichalcogenides. *Sci Rep* 2020;10(1).
- [10] Sverdlov V, El-Sayed A-M, Seiler H, Kosina H, Selberher S. Subbands in a nanoribbon of topologically insulating MoS<sub>2</sub> in the 1T' phase. *Solid-State Electron* 2021;184(1). <https://doi.org/10.1016/j.sse.2021.108081>.
- [11] Sverdlov V, Seiler H, El-Sayed A-M, Kosina H. Conductance due to the edge modes in nanoribbons of 2D materials in a topological phase. In: *Proc of 2021 Joint International EUROSIOI Workshop and International Conference on Ultimate Integration on Silicon (EuroSIOI-ULIS)*; 2021. p. 1–4. <https://doi.org/10.1109/EuroSIOI-ULIS53016.2021.9560173>.
- [12] Candido DR, Flatté ME, Egues JC. Blurring the Boundaries Between Topological and Nontopological Phenomena in Dots. *Phys Rev Lett* 2018;121(25).



**Viktor Sverdlov** received his Master of Science and PhD degrees in physics from the State University of St.Petersburg, Russia, in 1985 and 1989, respectively. From 1989 to 1999 he worked as a staff research scientist at the V.A.Fock Institute of Physics, St.Petersburg State University. During this time, he visited ICTP (Italy, 1993), the University of Geneva (Switzerland, 1993–1994), the University of Oulu (Finland, 1995), the Helsinki University of Technology (Finland, 1996, 1998), the Free University of Berlin (Germany, 1997), and NORDITA (Denmark, 1998). In 1999, he became a staff research scientist at the State University of New York at Stony Brook. He joined the Institute for Microelectronics, TU Wien, in 2004. His scientific interests include device simulations, computational physics, solid-state physics, and nanoelectronics.